Progress in Natural Science: Materials International 28 (2018) 520–528

HOSTED BY

Contents lists available at ScienceDirect

Progress in Natural Science: Materials International

journal homepage: www.elsevier.com/locate/pnsmi

Original Research

Numerical simulation for the investment casting process of a large-size titanium alloy thin-wall casing

Pan Tao[a], Heng Shao[a], Zhijun Ji[b], Hai Nan[b], Qingyan Xu[a,*]

[a] Key Laboratory for Advanced Materials Processing Technology, Ministry of Education, School of Materials Science and Engineering, Tsinghua University, Beijing, China
[b] Beijing Institute of Aeronautical Materials, Beijing, China

ARTICLE INFO

Keywords:
Titanium alloy
Investment casting
Numerical simulation
Finite difference method
Non-uniform mesh

ABSTRACT

To optimize the investment casting process when producing high quality large-size titanium alloy thin-wall components is a time-consuming job due to the complicated metallurgical process. Numerical simulation is a high-efficiency method compared with trial and error, and therefore is introduced to the investment casting process optimization to shorten the new product development cycle and reduce the production cost. In this study, weakly compressible model (WCM) and ununiformed finite difference mesh (UFDM) was developed to reduce the memory consumption and ensure the simulation efficiency. The precision of the WCM and UFDM were verified by numerical simulation of cavity heat convection in a square cavity and hydraulics simulation of centrifugal filling in a transparent cavity. The numerical simulation of the investment casting process of a titanium alloy thin-wall casing under different process conditions was accomplished using a self-developed software, and the distribution characteristics of potential shrinkage defects were predicted. It was found that the predicted defects in the titanium alloy casing matched well with the actual X-ray experimental results. For the components investigated in this paper, more numerical simulation results show that the centrifugal casting process with respect to gravity casting had no obvious improvements in the concentrated shrinkage defects, and the gravity casting process can be more reasonable from the engineering point of view.

1. Introduction

Due to excellent mechanical properties, corrosion resistance, heat resistance and biocompatibility, titanium alloy has been widely applied in the aerospace, chemical, medical equipment and other industries [1–5]. However, the cost of forming complex-shaped titanium alloy components is very high by traditional processing routes, which limits the application of titanium alloy components. The traditional method, forging + machining runs into problems when manufacturing shape-complicated thin-wall titanium alloy components as it is difficult to machine titanium alloy components, the process cycle is relatively long and the material utilization ratio is very low. Recently, the prosperous aerospace industry has led rapid growing demands for large-size shape-complicated thin-wall titanium alloy structural components for weight reduction consideration, which makes the process and quality control of large complex thin-walled titanium alloy parts come to the focus of attention. The emerging additive manufacturing (AM) is propitious to form free-shape components and the material utilization ratio is very high, but the AM is inappropriate to mass production because of its poor manufacturing efficiency and high processing cost [6–9]. The investment casting is suitable to form shape-complicated components with a relatively high efficiency. Besides, it enormously reduces machining work and related production cost. Accompanied with hot isostatic pressing (HIP), the porosities and small shrinkage cavities in titanium alloy castings can be effectively eliminated and the quality of the castings could be guaranteed.

The chemical activity of titanium alloy is extremely high, and therefore most titanium alloy is melt in a cold crucible. This leads to low superheat and poor filling capacity of the molten titanium alloy. While manufacturing shape-complicated large thin-wall structural titanium alloy components, insufficient pouring could be a serious challenge during investment casting for high cooling rate in thin-wall regions in the castings and poor filling capacity of titanium alloy. Thus centrifugal pouring is employed to strengthen the filling capacity and ensure completely filling [10]. Higher rotation speed is propitious to decrease the bubbles and shrinkage defects in the casting [11], but the maximum rotation speed is limited by the strength of the shell [12]. Shrinkage defects often appear in the development stage of shape-

Peer review under responsibility of Chinese Materials Research Society.
* Corresponding author.
E-mail addresses: taop14@mail.tsinghua.edu.cn (P. Tao), scjxqy@mail.tsinghua.edu.cn, scjxqy@tsinghua.edu.cn (Q. Xu).

https://doi.org/10.1016/j.pnsc.2018.06.005
Received 20 March 2018; Received in revised form 11 May 2018; Accepted 14 June 2018
Available online 01 August 2018

complicated components and some concentered shrinkage cavities are too big to be eliminated by subsequent HIP, which make the parts scrapped directly. The investment casting process involves many processes such as wax mold manufacturing and assembly, shell manufacturing, dewaxing and shell roasting, alloy melting and casting, and shell and casting cleaning and testing process and so on [13]. Due to the inherent complexity and time-consuming features of the investment casting process, the development of new products is bound to consume a lot of time and increase product cost only through experience or trial and error. Numerical simulation is introduced to the acceleration of process optimization to shorten the new product development cycle and reduce the cost of development.

Numerical simulation provides an alternative approach to research the investment casting process. Because it is much faster and cheaper than actual casting tests, the analysis of the casting process is no longer dependent solely on the experimental results. Numerical simulation has been widely used in practical casting process development up till now. The filling, solidification processes [14], defects formation and distribution characteristics during the investment casting process could be predicted before actual experiments. Liu et al. [15] investigated the influence of varying withdrawal rates on the microstructure of nickel-based super alloy blade castings during investment casting process, and the simulated results revealed the stray grains appeared at the edge of blades. Li et al. [16] developed a thermo-elastic-plastic model to analyze the plastic strains of a nickel-based single crystal alloy during directional solidification process, and predicted the recrystallization locations of simplified cored rods. Zhang et al. [17,18] simulated the grains competitive growth of a single crystal super alloy in the process of grain selection, and proposed design criteria for the spiral selector. At present, the research on numerical simulation of investment casting mainly focuses on the casting process of nickel-base alloy such as directional solidification processes. There is not too much research on the numerical simulation of investment casting of titanium alloy, especially the centrifugal casting process. Wang et al. [19] simulated the investment casting process of TiAl alloy blades and analyzed the effects of different blade inlet designs and blade orientations on the quality of the castings. Wu et al. [20] simulated the characteristics of shrinkage porosity in titanium castings during centrifugal casting and centrifugal casting process. Karwiński et al. [21] analyzed the velocity field and pressure field of titanium alloy in the centrifugal force during investment casting by numerical simulation. As the melt flow behavior in centrifugal casting is quite different from that in gravity casting and the formation of defects are also changed, the influence of centrifugal rotation need to be taken into account in centrifugal casting process design and optimization [22].

The popular SOLA-VOF method is a good solution for gravity casting simulation, but the efficiency rapidly decreases in the centrifugal casting simulation as the centrifugal rotation speed increases. In addition, the huge element number of shape-complicated thin-wall components further worsens the computational efficiency. The low efficiency of numerical simulation brings adverse effects on the engineering application of centrifugal casting of complex thin-walled components. Therefore, it is necessary to further study and improve the existing numerical simulation methods. In this paper, a software based on the WCM and the UFDM has been developed to improve the efficiency of centrifugal casting simulation for large-size thin-wall parts because the efficiency of the WCM is only slightly affected by rotation and the UFDM can significantly reduce the amount of elements. The numerical simulation of investment casting of a large-size thin-wall titanium alloy casing was accomplished based on the self-developed software and the filling, solidification process and defects in this component were predicted. The predicted shrinkage defects matched well with X-ray detection results.

2. Mathematical model of numerical simulation for investment casting

2.1. The filling and solidification process model

As the software is developed for both centrifugal casting and gravity casting, centrifugal casting is considered as the general situation. The movement of the metal melt during centrifugal casting is not only affected by gravity, but also by the centrifugal force and the Coriolis force so that the melt flow process is more complex and changeable than in gravity casting. According to the flow phenomena in the case of centrifugal rotation, the WCM is applied to ensure the calculation efficiency. The momentum conservation equation and mass conservation equation in the coordinate system fixed on the casting mold are

$$\frac{\partial u}{\partial \tau} + u\frac{\partial u}{\partial x} + v\frac{\partial u}{\partial y} + w\frac{\partial u}{\partial z} = -\frac{1}{\rho}\frac{\partial p}{\partial x} + \frac{\mu}{\rho}\nabla^2 u + g_x \tag{1}$$

$$\frac{\partial v}{\partial \tau} + u\frac{\partial v}{\partial x} + v\frac{\partial v}{\partial y} + w\frac{\partial v}{\partial z} = -\frac{1}{\rho}\frac{\partial p}{\partial y} + \frac{\mu}{\rho}\nabla^2 v + g_y \tag{2}$$

$$\frac{\partial w}{\partial \tau} + u\frac{\partial w}{\partial x} + v\frac{\partial w}{\partial y} + w\frac{\partial w}{\partial z} = -\frac{1}{\rho}\frac{\partial p}{\partial z} + \frac{\mu}{\rho}\nabla^2 w + g_z \tag{3}$$

$$\frac{\partial \rho}{\partial \tau} + \frac{\partial(\rho u)}{\partial x} + \frac{\partial(\rho v)}{\partial y} + \frac{\partial(\rho w)}{\partial z} = 0 \tag{4}$$

$$g_x = \omega^2 x + 2\omega v \tag{5}$$

$$g_y = \omega^2 y - 2\omega u \tag{6}$$

$$g_z = g \tag{7}$$

where u, v and w are the components of velocity in X, Y and Z direction, g_x, g_y and g_z are the components of body force in the 3 directions, τ is time, ρ is the density of the fluid, P is the pressure, μ is the kinematic viscosity, ω is the angular velocity of the rotating coordinate system, and g is gravity acceleration.

The energy conservation equation is

$$\rho c\frac{\partial T}{\partial \tau} + \rho c u\frac{\partial T}{\partial x} + \rho c v\frac{\partial T}{\partial y} + \rho c w\frac{\partial T}{\partial z} = \frac{\partial}{\partial x}\left(k\frac{\partial T}{\partial x}\right) + \frac{\partial}{\partial y}\left(k\frac{\partial T}{\partial y}\right) + \frac{\partial}{\partial z}\left(k\frac{\partial T}{\partial z}\right) + S \tag{8}$$

where c is the equivalent specific heat capacity, k is the heat conductivity, T is the temperature, and S is the source term. Equivalent specific heat capacity means when the melt is solidifying, latent heat will be treated as extra specific heat capacity.

The density of the fluid is related to the pressure. It is assumed that the fluid has a certain degree of compressibility in the WCM. For the metal melt, the effect of temperature on the density of metals is negligible except at the solidification stage. The state equation is

$$p = p_0 + K(\rho - \rho_0)/\rho_0 \tag{9}$$

Where p_0 is the reference pressure, which is taken as atmospheric pressure, ρ_0 is the actual density of the fluid, and K is the modulus of compression. With an appropriate K, the calculated ρ is only slightly deviated from ρ_0 and the precision of numerical simulation can be guaranteed.

In view of that fact that the time step required for the flow field calculation is much smaller than that for the calculation of the temperature field, the convective term in the energy equation is often separately from the heat conduction term, meaning that the calculation of convection term is conducted in the time step required for the flow field and the calculation of heat conduction term is performed in a large time step.

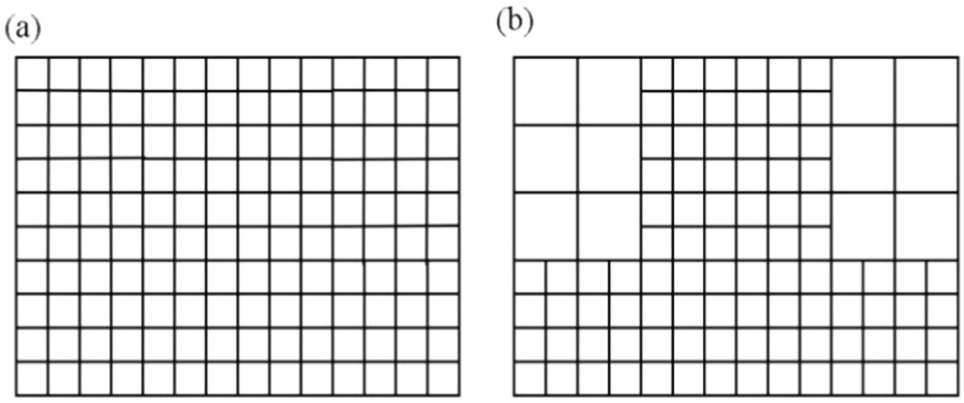

Fig. 1. Schematic of the uniformed (a) and the ununiformed (b) finite difference mesh.

2.2. Ununiformed finite difference mesh

Thin-wall structures play a very important role in many titanium alloy components for aerospace uses. On the other hand, the pouring system must be thick enough to insure complete filling. A small mesh size, which means a huge number of elements in the simulation for a large-size thin-wall casting if using uniform meshing as shown in Fig. 1(a), is needed to describe the shape of a thin-wall casting accurately. In order to decline the amount of elements, the UFDM is applied in the simulation for a large-size thin-wall casing: the small mesh size is applied in the thin-wall structure to describe the detail geometric features and the big mesh size is applied in other thick parts such as the pouring system to reduce the quantity of elements.

In traditional ununiformed finite difference mesh, the neighboring meshes have a 1 on 1 interface. The advantage is that the interface processing is relatively simple, but the disadvantages are that the lengths of the mesh in different directions may be quite different and the size of a mesh element is not free: mesh elements which have a common x-coordinate also have a common Δx, and the same goes for Δy and Δz.

In the present study, a 1–4 interface is applied on the boundary between big mesh region and small mesh region to decouple the mesh sizes of elements in the 2 regions. As shown in Fig. 1(b), some mesh elements having a common height coordinate have different size in height direction, and some other mesh elements having a common horizontal coordinate have different size in horizontal direction. These means the decision of the mesh size gets a greater freedom. Accordingly, a transition region is applied to solve the flow across the 1–4 interface when a big mesh meets a small mesh. Fig. 2(a) shows the transition region between a big mesh and a small mesh.

The mesh size of Mesh 1 is two times as big as that of Mesh 2 and each element in Mesh 1 meats 4 elements in Mesh 2. Mesh 1 has an extension named Mesh 2′ (big mesh) to read data from Mesh 2. Mesh 2 correspondingly has an extension named Mesh 1′ (small mesh). During the simulation, the calculation on Mesh 1 is based on data on Mesh 1 and 2′ and the calculation on Mesh 2 is based on data on Mesh 2 and 1′. After the calculation, data on Mesh 1 and 2 are refreshed. Before a new round of calculation, data on Mesh 1′ and 2′ also need to be refreshed.

As the mesh sizes of Mesh 1 and Mesh 2 are different, the management of variables on the transition region is very important. Fig. 2(b) displays the 2-D schematic of the management. The non-uniformity of local density and specific heat capacity is ignored. First, Mesh 2′ (big mesh) read data from Mesh 2 (small mesh)

$$u_{B,\,\mathrm{i+3/2,\,j+1/2}} = \frac{1}{2}\left(u_{S,\,\mathrm{i+3/2,\,j}} + u_{S,\,\mathrm{i+3/2,\,j+1}}\right) \tag{10}$$

$$v_{\mathrm{B,\,i+5/2,\,j-1/2}} = \frac{1}{2}\left(v_{S,\,\mathrm{i+2,\,j-1/2}} + v_{S,\,\mathrm{i+3,\,j-1/2}}\right) \tag{11}$$

$$p_{B,\,\mathrm{i+5/2,\,j+1/2}} = \frac{1}{4}(p_{S,\,\mathrm{i+2,\,j}} + p_{S,\,\mathrm{i+3,\,j}} + p_{S,\,\mathrm{i+2,\,j+1}} + p_{S,\,\mathrm{i+3,\,j+1}}) \tag{12}$$

$$T_{B,\,\mathrm{i+5/2,\,j+1/2}} = \frac{1}{4}(T_{S,\,\mathrm{i+2,\,j}} + T_{S,\,\mathrm{i+3,\,j}} + T_{S,\,\mathrm{i+2,\,j+1}} + T_{S,\,\mathrm{i+3,\,j+1}}) \tag{13}$$

where the B/S in subscript means big mesh or small mesh, and the other two mean the position: integer means the center of small mesh and half means the border.

Second, Mesh 1′ (small mesh) reads data from Mesh 1 (big mesh):

$$W_{\mathrm{S}} = W_{\mathrm{B}} + \frac{\partial W}{\partial x}\Delta x + \frac{\partial W}{\partial y}\Delta y \tag{14}$$

$$\frac{\partial W}{\partial x}\Big|_{i+1/2,\,j+1/2} = \frac{1}{2\delta x}(W_{B,\,\mathrm{i+3/2,\,j+1/2}} - W_{B,\,\mathrm{i-1/2,\,j+1/2}}) \tag{15}$$

$$\frac{\partial W}{\partial y}\Big|_{i+1/2,\,j+1/2} = \frac{1}{2\delta y}(W_{B,\,\mathrm{i+1/2,}j+3/2} - W_{B,\,\mathrm{i+1/2,\,j-1/2}}) \tag{16}$$

where W represents u, v, p or T, δx and δy are the mesh sizes on direction X and Y, and Δx & Δy are the relative position of the variables on the small mesh to the variables on the nearest big mesh.

If the requested velocity on small mesh locates inside a big mesh rather than on the border of a big mesh, W_{B} should be

$$u_{B,\,\mathrm{i+1/2,\,j+1/2}} = \frac{1}{2}(u_{\mathrm{B,\,i-1/2,\,j+1/2}} + u_{\mathrm{B,\,i+3/2,\,j+1/2}}) \tag{17}$$

$$v_{B,\,\mathrm{i+1/2,\,j+1/2}} = \frac{1}{2}(v_{B,\,\mathrm{i+1/2,\,j-1/2}} + v_{B,\,\mathrm{i+1/2,\,j+3/2}}) \tag{18}$$

3. Verification of the precision of the software

3.1. Verification of the UFDM

The UFDM significantly decreases the number of elements, memory consumption and calculation time, leading to higher calculation efficiency. However, different mesh would more or less influence the simulation result. Thus the precision of the UFDM would be verified by comparing simulation results on different meshes.

The calculation domain is a square cavity shown in Fig. 3(a). The length of the cavity is L, and the temperatures of the left wall and right wall are T_{h} and T_{c}. The other walls are adiabatic. The cavity is full of liquid, whose density is ρ, dynamic viscosity is ν, thermal expansion coefficient is β, and thermal diffusivity is α. The flow is driven by buoyancy g_{b} and Eq. (7) is replaced by

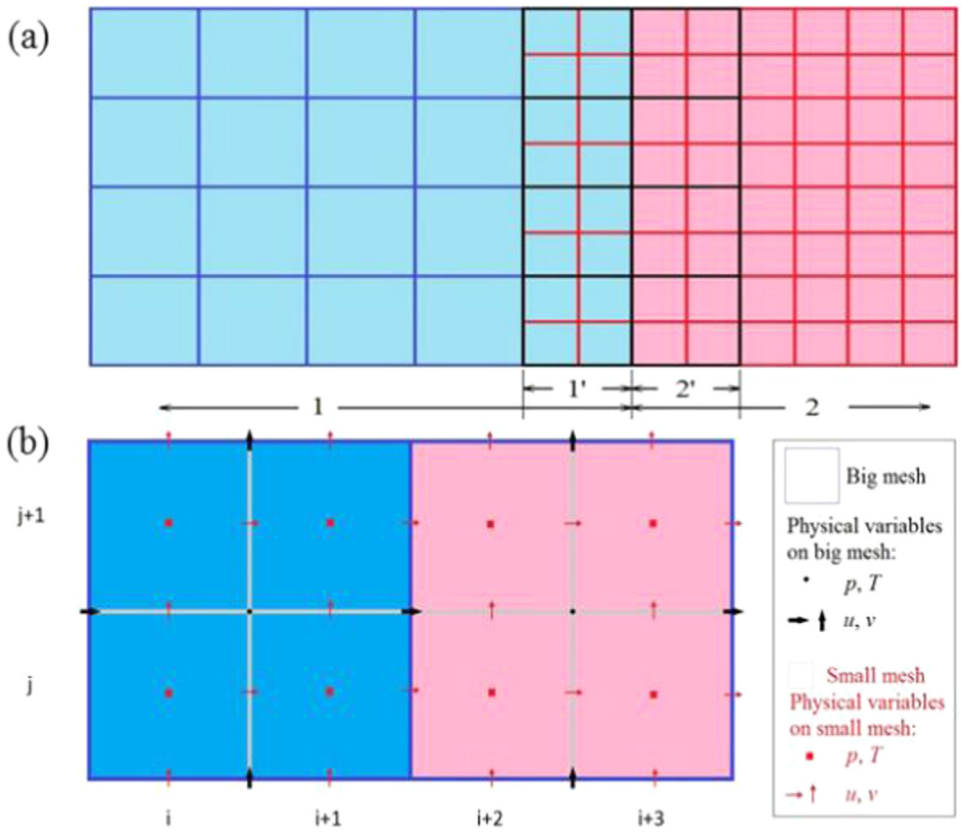

Fig. 2. (a) Transition region between a big mesh (Mesh 1) and a small mesh (Mesh 2) and (b) 2-D schematic of the management of variables on the transition region.

$$g_z = g_b = \beta\left(\frac{T_h + T_c}{2} - T\right)g \tag{19}$$

The UFDM shown in Fig. 3(b) is applied in the heat convection simulation. Simulation on uniform mesh of big size or small size has also been accomplished as references.

Simulation results on the UFDM, big mesh and small mesh are shown in Fig. 4, in which $\bar{\tau} = \tau\alpha/L^2$. Corresponding conditions are: Rayleigh number Ra ($=g\beta\ (T_h\text{-}T_c)L^3\rho/\alpha\mu$) $= 10^7$ and the mesh sizes of the small mesh and big mesh are $L/200$ and $L/100$, respectively. The simulation results on UFDM are in the range of the simulation results on uniform grid with small size and uniform grid with large size, indicating that the UFDM has no significant effects on the precision of simulation results.

3.2. Validation by hydraulics simulation

As the kinematic viscosity of water is close to that of molten metal, the flow state of molten metal in casting mold is similar to that of water in transparent mold. In the present study, the comparison between numerical simulation and hydraulics simulation has been accomplished to verify the precision of the numerical simulation further. Fig. 5 is the schematic of the mold in hydrodynamic simulation.

The mold kept rotating at 150 rpm in clockwise direction when colored water was poured into the cavity (pouring time was 3.3 s). The flow state of water was recorded by high-speed camera and numerical simulation under corresponding conditions was also done. The comparison between numerical simulation result and recorded flow state at different time is shown in Fig. 6.

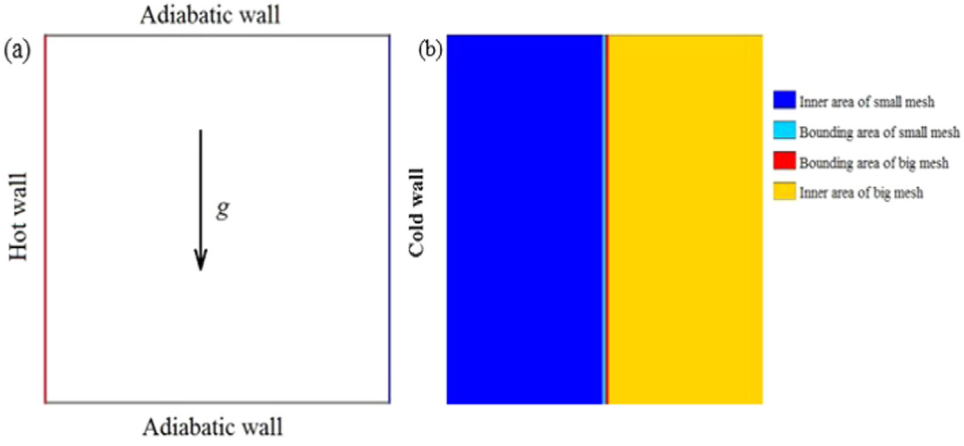

Fig. 3. (a) The calculation domain for the simulation of heat convection and (b) the schematic of the UFDM for heat convection simulation.

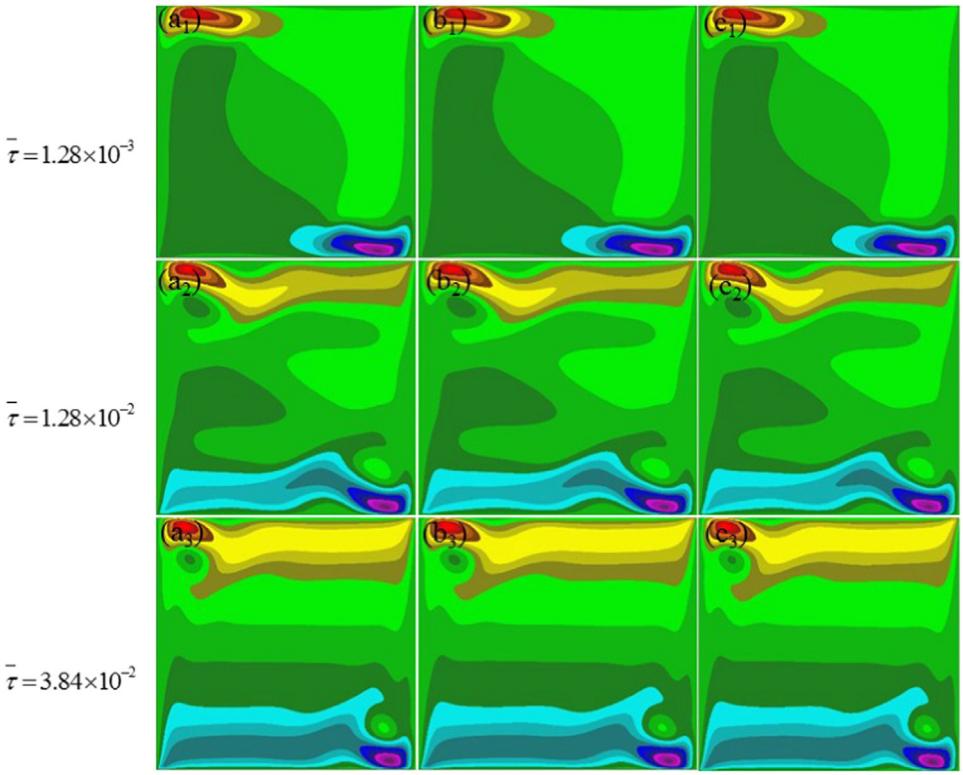

Fig. 4. Simulated horizontal velocity u field on different mesh (a) Small mesh, (b) The UFDM, (c) Big mesh.

The results in Fig. 6 indicate that the numerical simulated flow state matches well with the recorded experimental results. Both the shape of the free surface and filling rate in the simulation result are similar to the recorded experimental result. Thus the precision of filling simulation result is verified further.

4. Numerical simulation of investment casting of a casing

4.1. Original process

Fig. 7 illustrates the geometric model of casing and its pouring system. The overall dimension of the casing was Φ660 mm × 720 mm with a minimum thickness of 8 mm. The original process was gravity casting. The used material was Ti-6Al-4V alloy, whose liquidus temperature (T_L) and solidus temperature (T_S) are 1650 °C and 1600 °C, respectively. The temperature-dependent thermo-physical parameters of the casting and the mold are used according to the references [23,24]. The related simulation and process parameters are shown in Table 1.

Fig. 8 shows the simulated filling process at 3.9 s, solidification temperature field at 40 s and residual shrinkage holes in the casing under original process condition. The simulated results indicate that the melt can flow smoothly and fill the cavity gradually from bottom to top until the whole cavity is filled completely under current process parameters. The temperature of the vast majority of the casing is higher than 1650 °C during the filling process. After filling, the casing cooled down gradually. The top part of the inner wall of the casing cooled more slowly than the outer wall. Thus the attachments on the outer wall of the casing influenced the cooling process. The outer surface of the top flange and the cylindrical bosses in the middle region of casing were completely solidified after 40 s, but some regions such as the triangular bosses and rectangular bosses as shown in the black circle in Fig. 8(b) still had a higher temperature than the solidus of Ti-6Al-4V alloy. So the casing is not evenly cooled during solidification. The casing is solidified in layers, which makes most of liquid part of the casing separated from the pouring system during solidification. As a result, shrinkage holes would appear in the separated liquid part for lack of liquid feeding. The simulated shrinkage defects in the casing are shown in Fig. 8(c). There were different sizes of shrinkage cavities distributed in the casing. The biggest holes appeared in the top of casing and smaller holes were mainly distributed in the cylindrical bosses. The triangular bosses and rectangular bosses solidified slowly for larger thickness and were easily isolated from other regions, resulting in big concentrated shrinkage cavities in the bosses. Because the lower part of the casing solidified slowly and could be fed effectively, the concentrated shrinkage defects were mainly located in the upper part of the casing. These small size

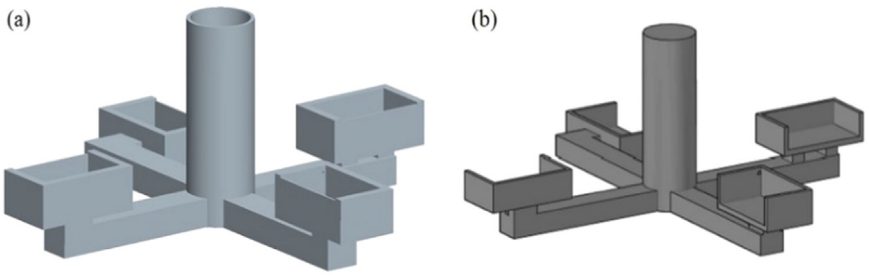

Fig. 5. Schematic of the mold (a) and its inner cavity (b) for hydraulics simulation.

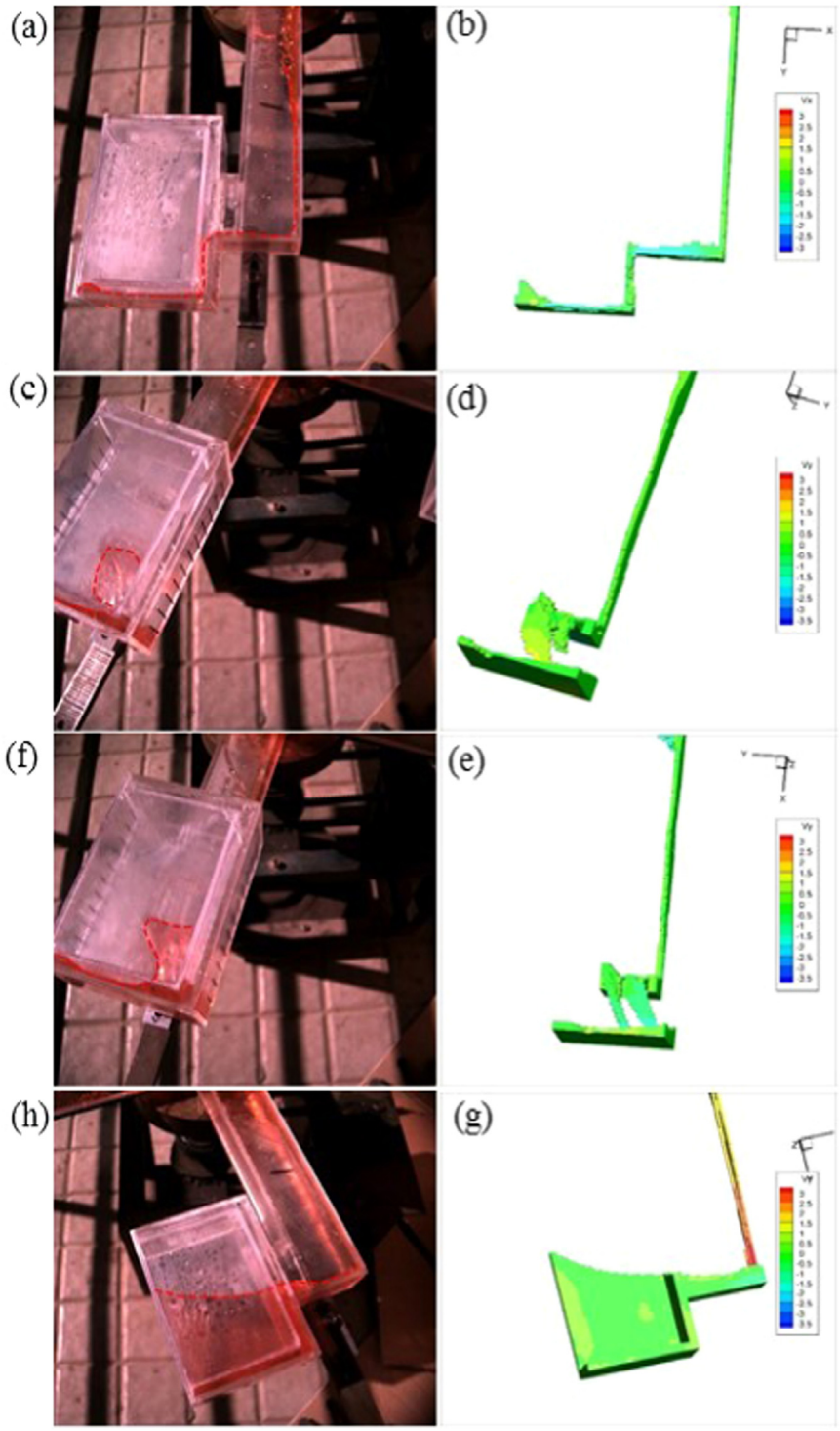

Fig. 6. Numerical simulated result and recorded flow state at different time: (a) (c) (e) (g) are recorded flow state after 0.483 s, 0.748 s, 0.889 s and1.560 s from the beginning of pouring, respectively; (b) (d) (f) (h) are recorded flow state after 0.5 s, 0.8 s, 0.9 s and1.6 s from the beginning of pouring, respectively.

holes in the casing might be eliminated after HIP, but the big shrinkage cavities are difficult to be removed. Therefore, the current casting process cannot be applied to the actual production and needs to be optimized.

4.2. Modified processes

As big shrinkage holes would appear in the casing in original casting process and deteriorate the quality of the casing, some process modification is needed to avoid the big holes. The first improvement scheme is adding some feeders near the biggest holes in the inner wall of the casing to remove the shrinkage holes. The casting process in Scheme 1 is still gravity casting. The casting process parameters in Scheme 1 is the same as the original process. As centrifugal casting could promote the effect of feeding, centrifugal rotation with 200 rpm rotational speed is added based on Scheme 1 in Scheme 2 in order to diminish other smaller holes.

Fig. 9 shows the simulated filling, the solidification temperature

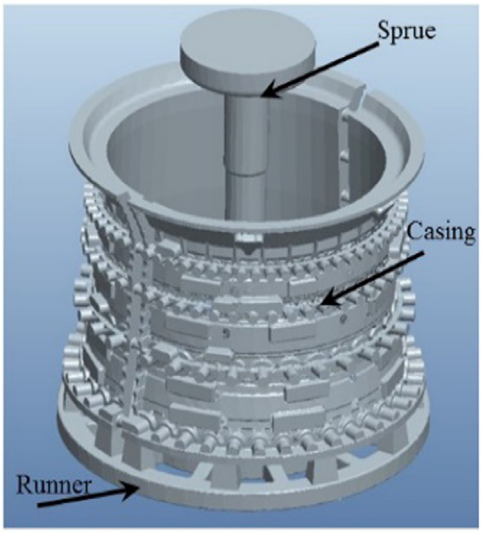

Fig. 7. 3-D model of the casing and its pouring system.

Table 1
The simulation parameters of Ti-6Al-4V alloy casing in original process.

Parameters	Values
Pouring temperature (°C)	1720
Shell preheating temperature (°C)	200
Pouring time (s)	5.5
Centrifugal rotation speed (r/min)	0
Interfacial heat-transfer coefficient between casting and mold ($W m^2 k^{-1}$)	[25]
Mesh size (mm)	2 mm, 4 mm
Element number for casting	1593129(2 mm), 219566(4 mm)
Element number for mold	2799935(2 mm), 163000(4 mm)

field and the distribution of concentrated shrinkage holes of the casing in Scheme 1 and Scheme 2. The only difference between original process and Scheme 1 is the feeders, and the same goes for the filling processes. The feeders disturb the melt flow during filling. Thus the surface of the melt becomes wavy after the feeders are filled, as shown in Fig. 9(a)$_1$. Compared to the original process, the additional feeders can be used to supplement the liquid melt for the isolated liquid regions around them. As a result, the biggest shrinkage holes are moved into the feeders as shown in Fig. 9(c)$_1$, but smaller holes far away from the feeders are almost unchanged. The shrinkage holes in the feeders are oriented along the direction of gravity. The big concentrated defects in the casing could be removed basically in the Scheme 1 with respect to the original process.

Compared to the above gravity casting processes, the filling of the casing in the centrifugal casting process becomes significantly faster and the free surface goes out of flatness under the action of centrifugal force. The cavity is almost completely filled at 3.9 s and the melt reaches the top of the casing far ahead of the end of filling as shown in Fig. 9(a)$_2$. The last filling regions in the centrifugal casting are the feeders instead of the top flange of the casing in gravity casting process. The solidification seems a little faster than that in Scheme 1 and the original process because the filling of the casing is earlier. The characteristics of shrinkage holes are quite different: the number of biggest holes in the feeders declines and average volume becomes bigger (Fig. 9c$_2$). The biggest holes in feeders are oriented toward the centrifugal rotation center. Besides, the smaller holes in the casing seem to become bigger. The thickness of the top of the casting is greater than that of the middle, and the solidification rate is slower. Since the symmetrical arrangement of the casting is not a complete circular structure, the joint region is closer to the centrifugal axis than the other regions. In addition, liquid areas are separated and far away from each other in the thin-wall casing during solidification. Thus centrifugal force promotes feeding in one separated liquid area rather than among the separated liquid areas. Although centrifugal rotation can reduce the bubbles and shrinkage defects in the casting, it does not necessarily apply to all cases. The suitability of centrifugal casting is based on the geometry of the part.

Compared to the Scheme 1, the centrifugal casting process has no obvious improvements in the concentrated defects in the casing and needs a higher strength of shell and complex process control, which would increase the additional cost of production. Thus the gravity casting process is enough to produce the compressor casing. In the above 3 Schemes, the small defects in the cylinder bosses are difficult to eliminate or minish because of larger size feature. After HIP, these small defects may disappear. But the press pits may appear on the surface of casing, which could be fixed by welding.

4.3. Experimental results

Fig. 10 shows the X-ray photographs and corresponding simulation results in original process and Scheme 1. Fig. 10(a)$_1$~a$_2$, b$_1$~b$_2$ and c$_1$~c$_2$ display the X-ray results of shrinkage holes on the left, middle and right side of the casing. Fig. 10(d)$_1$~d$_2$ show the simulated concentrated shrinkage defects in original process and Scheme 1.

From the X-ray results, the amount of defects in Scheme 1 declines obviously with respect to the original process, which indicates that the process modification in Scheme 1 is reasonable. The simulation illustrates that there are shrinkages holes in the cylinder bosses, and some

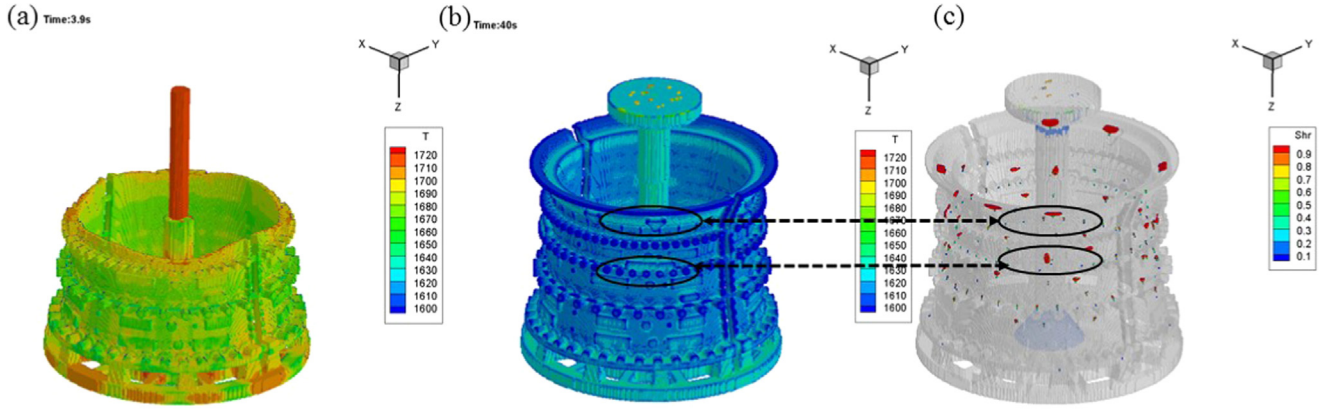

Fig. 8. Simulated filling (a), solidification temperature field (b) of the casing in original process from the beginning of filling and simulated shrinkage holes in the casing (c).

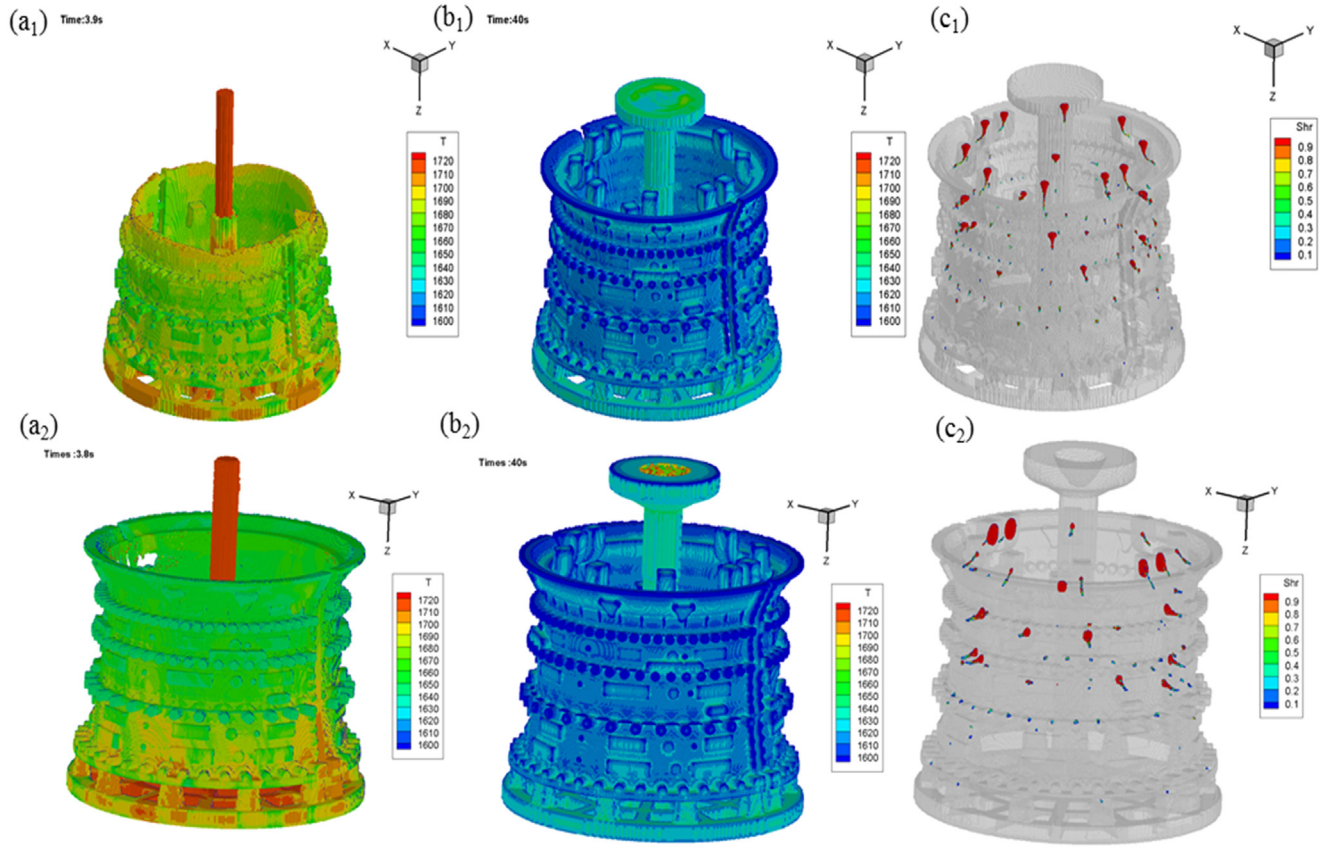

Fig. 9. Simulated results of the casing in the modified processes: (a_1) (b_1) (c_1) simulated filling, temperature field and shrinkage defects of the casing in Scheme 1; (a_2) (b_2) (c_2) simulated filling, temperature field and shrinkage defects of the casing in Scheme 2.

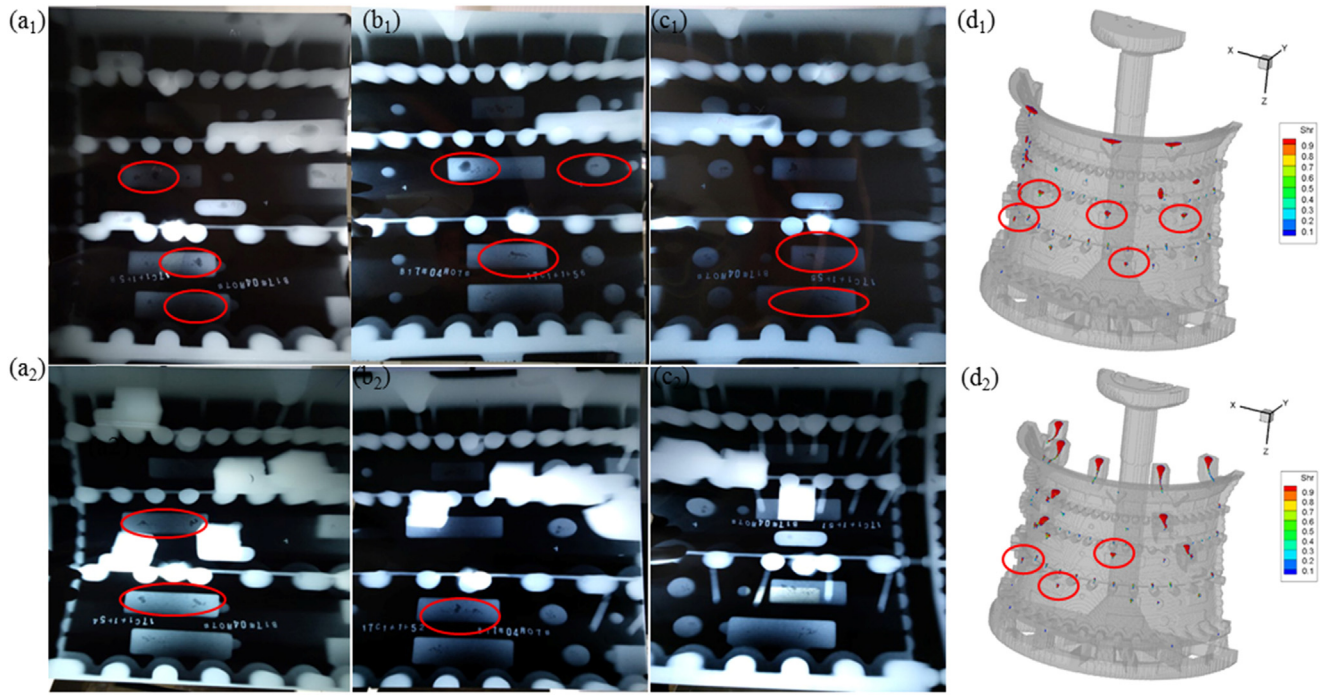

Fig. 10. X-ray photographs and corresponding simulation result in original process and Scheme 1: (a_1-a_2) left side, (b_1-b_2) middle, (c_1-c_2) right side of the casing, and (d_1-d_2) the simulation result of concentrated shrinkage defects.

other holes in the thickened rectangles in the casing. Holes in the cylinders are hidden in the X-ray photographs because the length of the cylinders is much bigger than the thickness of the casing, while holes in the rectangles are clearly displayed and match well with the experiment results.

5. Conclusion

The investment casting process of a large-size titanium alloy thin-wall casing has been simulated by self-developed software using WCM and UFDM method. The filling, solidification temperature field and shrinkage holes in different process schemes have been investigated, and the shrinkage holes in titanium alloy casing analyzed using X-ray testing. Based on the above experimental results and simulation analysis, the following conclusions can be drawn:

(1) The WCM provides a good accuracy in the flow simulation under centrifugal rotation. The UFDM keeps the accuracy while significantly declining the mesh number, memory occupancy and simulation time.
(2) The predicted shrinkage defects match well with the X-ray experiment results.
(3) Feeders are effective in eliminating shrinkage holes in the casing under gravity casting while additional centrifugal rotation has no obvious improvements in the concentrated defects in the casing. The reason is that the casing is too thin for centrifugal force to promote feeding. The gravity casting is more suitable than centrifugal casting for manufacturing this compressor casing from the actual production point of view.

Acknowledgments

This work has received funding from innovation programme under grant agreement No. 690725 (EMUSIC), the European Union's Horizon 2020 research; MIIT under the program number MJ-2015-H-G-104; the National Natural Science Foundation of China (Nos. 51374137, 51171089).

References

[1] S.L. Xiao, Y.Y. Chen, H.Y. Zhu, et al., Rare Met. Mater. Eng. 35 (2006) 678–681.
[2] H. Jia, F.S. Lu, B. Hao, Titan. Ind. Progress. 34 (2017) 1–7.
[3] D.D. Zhao, Foundry 63 (2014) 1114–1117.
[4] J.C. Williams, E.A. Starke Jr., Acta Mater. 51 (2003) 5775–5799.
[5] D. Banerjee, J.C. Williams, Acta Mater. 61 (3) (2013) 844–879.
[6] L.C. Zhang, H. Attar, M. Calin, et al., Mater. Technol. 31 (2) (2016) 66–76.
[7] Y. Huang, M.C. Leu, J. Mazumder, et al., J. Manuf. Sci. Eng. 137 (2015) 014001.
[8] N. Guo, M.C. Leu, Front. Mech. Eng. 8 (2013) 215–243.
[9] W. Gao, Y. Zhang, D. Ramanujan, et al., Comput.-Aided Des. 69 (2015) 65–89.
[10] R. Yang, Y.Y. Cui, Q. Jia, et al., Aerosp. Mater. Technol. 3 (2013) 56–59.
[11] K. Suzuki, M. Yao, Met. Mater. Int. 10 (2004) 33–38.
[12] Y.D. Chu, H. Chang, D. Huang, et al., Spec. Cast. Nonferrous Alloy. 32 (2012) 133–136.
[13] Z.Z. Fan, X.L. Xu, Y.L. Wang, et al., (Liu), Spec. Cast. Nonferrous Alloy. 34 (2014) 285–289.
[14] Z. Liang, Q.Y. Xu, J. Li, et al., Acta Metall. Sin. 40 (2004) 439–444.
[15] B.C. Liu, Q.Y. Xu, T. Jing, et al., JOM 63 (2011) 19–25.
[16] Z. Li, J. Xiong, Q. Xu, et al., J. Mater. Process. Technol. 217 (2015) 1–12.
[17] H. Zhang, Q. Xu, C. Sun, et al., Acta Metall. Sin. 49 (12) (2013) 1508–1520.
[18] H. Zhang, Q. Xu, C. Sun, et al., Acta Metall. Sin. 49 (12) (2013) 1521–1531.
[19] H. Wang, G. Djambazov, K.A. Pericleous, et al., Comput. Fluids 42 (2011) 92–101.
[20] M.H. Wu, J. Schädlich-Stubenrauch, M. Augthun, et al., Dent. Mater. 14 (1998) 321–328.
[21] A. Karwiński, W. Lesniewski, P. Wieliczko P, M. Małysza, Arch. Metall. Mater. 59 (2014) 403–406.
[22] S.P. Wu, J.J. Guo, J. Jia, Acta Metall. Sin. 40 (2004) 326–330.
[23] K.C. Mills, Recommended values of thermophysical properties for selected commercial alloys, Woodhead Publishing, 2002.
[24] H. Shao, Z. Luo, Y. li, et al., Foundry (2014) 2.
[25] H. Shao, Y. li, H. Nan, et al., Acta Metall. Sin. 51 (8) (2015) 976–984.